Reduction and carburization of iron oxides for Fischer-Tropsch synthesis

Monia Runge Nielsen[a], Asger Barkholt Moss[a,b], Anton Simon Bjørnlund[a,b], Xi Liu[c,d], Axel Knop-Gericke[e,f], Alexander Yu. Klyushin[e,g], Jan-Dierk Grunwaldt[h,i], Thomas L. Sheppard[h,i], Dmitry E. Doronkin[h,i], Anna Zimina[h,i], Thomas Eric Lyck Smitshuysen[b], Christian Danvad Damsgaard[a,b], Jakob Birkedal Wagner[a], Thomas Willum Hansen[a,*]

[a]*DTU Nanolab, Technical University of Denmark, DK-2800 Kgs. Lyngby, Denmark*

[b]*Department of Physics, Technical University of Denmark, DK-2800 Kgs. Lyngby, Denmark*

[c]*SynCat@Beijing, Synfuels China Technology Co., Ltd, Beijing 101407, China*

[d]*School of Chemistry and Chemical Engineering, Shanghai Jiao Tong University, Shanghai 200240, China*

[e]*Department of Inorganic Chemistry, Fritz Haber Institute of the Max Planck Society, D-14195 Berlin, Germany*

[f]*Research Group Heterogeneous Reactions, Max Planck Institute for Chemical Energy Conversion, D-45470 Mülheim, Germany*

[g]*Research Group Catalysis for Energy, Helmholtz-Zentrum Berlin for Materials and Energy (BESSY II), D-12489 Berlin, Germany*

[h]*Institute for Chemical Technology and Polymer Chemistry, Karlsruhe Institute of Technology, D-76131 Karlsruhe, Germany*

[i]*Institute of Catalysis Research and Technology, Karlsruhe Institute of Technology, D-76344 Eggenstein-Leopoldshafen, Germany*

*Corresponding author. E-mail address: thwh@dtu.dk (T. W. Hansen).

Abstract

The activation of iron oxide Fischer-Tropsch synthesis (FTS) catalysts was investigated during pretreatment: reduction in hydrogen followed by carburization in either CO or syngas mixture, or simultaneously reduction and carburization in syngas. A combination of different complementary *in situ* techniques was used to gain insight into the behavior of Fe-based FTS catalysts during activation. *In situ* XRD was used to identify the crystalline structures present during both reduction in hydrogen and carburization. An increase in reduction rate was established when increasing the temperature. A complete reduction was demonstrated in the ETEM and a grain size dependency was proven, i.e. bigger grains need higher temperature in order to reduce. XPS

and XAS both indicate the formation of a small amount of carbonaceous species at the surface of the bulk metallic iron during carburization.
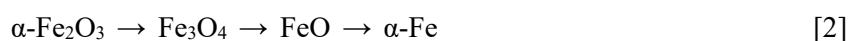
1.Introduction

Fischer-Tropsch Synthesis (FTS) is a catalyzed chemical reaction, in which synthesis gas (syngas), a mixture of carbon monoxide (CO) and hydrogen (H_2) obtained from either coal, biomass or natural gas, is converted into mainly hydrocarbons (linear paraffins and primary olefins), with various amounts of oxygenates (alcohols, aldehydes, ketones and acids), which are subsequently used for making liquid fuels and chemicals [1]. Most group VIII metals are known to be active components in the FTS reaction, but only iron (Fe) and cobalt (Co) are typically used industrially [2]. Compared to cobalt (operational temperatures <240 °C), iron (typically used for short-chain olefins at >300 °C) is cheaper as it is one of the most abundant elements in the crust of the earth. Iron catalysts are less active but also less impacted by operating conditions, i.e. pressure and temperature. As a result of this, they are less sensitive towards sintering [3,4]. They are good water-gas shift (WGS) catalysts, and they are the preferred catalysts when coal, with a low hydrogen to carbon ratio, is the source of syngas [3]. These advantages make the Fe-based catalysts an attractive candidate in the development of next generation FTS catalysts. The Fe-based FTS catalyst is one of the most studied systems [5] in the field of heterogeneous catalysis. However, even after more than 90 years of research, the structural composition of the active sites is still under discussion [6]. During activation of the Fe-based catalysts and subsequent FTS, a complex mixture of iron phases is present [7-9]. In general, it is recognized that iron oxides, metallic iron and carbidic iron coexist after activation and during FTS. Surface carbidic iron has been suggested to be the active phase [10]. Nevertheless, even after great effort in characterizing the active phase, the exact identity of the active catalytic phase remains controversial.

Iron oxide is an important precursor in FTS catalysts. It is well known that magnetite catalyzes the water-gas shift reaction [11], and it is considered to be the phase responsible for the WGS activity of the Fe-based FTS catalyst [11-16]. It is generally accepted in literature that the WGS reaction and the FTS reaction takes place on different active sites of the catalyst. Since magnetite is known to co-exist with other iron phases during FTS, it plays an important role in determining the overall activity and selectivity of the catalyst. Magnetite has even been suggested to be the active phase in FTS [17-19].

The reduction mechanism of iron oxides has been studied extensively over the last century [20-23]. It is generally accepted that the water content affects the reduction kinetics [20-26]. Wimmers et al. [22] used Temperature Programmed Reduction (TPR) to investigate the reduction of hematite particles. They observed that the reduction rate is affected by H_2O and concluded that water inhibits the reaction significantly. This is confirmed by Zielinski et al. [23], who investigated the effect of water on the reduction path for hematite in pure H_2. They showed that not only water inhibited the hematite reduction, but the water content also determined whether or not the reduction path occurred in two (low water content) or three steps (high water content), where the two step process is the most favorable below 570 °C [23]:

$$\alpha\text{-Fe}_2O_3 \rightarrow Fe_3O_4 \rightarrow \alpha\text{-Fe} \qquad [1]$$

$$\alpha\text{-Fe}_2O_3 \rightarrow Fe_3O_4 \rightarrow FeO \rightarrow \alpha\text{-Fe} \qquad [2]$$

This is further supported by Rau [27] and Barin [28] who noticed that the three step reduction process only takes place at temperatures above 570 °C and at $(X_{H2O})/(X_{H2})$ ratios above 0.35. Lorente et al. [20] found that the first reduction step ($\alpha\text{-Fe}_2O_3 \rightarrow Fe_3O_4$) is not affected by water. However, further reduction is significantly inhibited even at the lowest content of water. Kock et al. [29] reported that if the hydrogen to water ratio falls below 1, complete reduction to metallic iron becomes impossible, even at 1000 °C. For that reason, it can be advantageous to use gaseous CO as the reducing gas instead of H_2.

It was first noted by Levy and Boudart [30] that carbides of tungsten catalytically behave similar to platinum by catalyzing the reaction of H_2 and O_2 at room temperature. Often studies of the activity, selectivity and resistance to poisoning of transition metal carbides (TMCs) surpass the properties of the best known group VIII catalysts for hydrogenation reactions [31]. TMC compounds are therefore promising heterogeneous catalysts due to their enhanced attrition (i.e. breaking up of catalyst particles into smaller particles) and sintering (i.e. loss of catalytically active surface area) resistance [32].

Even though it has been observed experimentally that carburized iron is an active catalyst [33], it is still disputed in literature whether or not bulk carbide phases play an active role in the FTS [34]. The question is why iron forms bulk carbides under FTS conditions, when the other active metals do not, this has been addressed by Niemantsverdriet and colleagues [34]. All phases have been claimed to be the active phase in FTS reactions [35].

In order to gain deeper insight into the activation behavior of Fe-based FTS catalysts, a better understanding of the structure and of the role of the different iron species formed during the different stages of reaction is

needed. Since the sensitivity of the Fe-based catalysts to oxidation by air is well known [36], a combination of complementary *in situ* techniques were used to investigate the activation of iron oxide for the Fischer-Tropsch synthesis. Iron oxide is typically activated in either hydrogen (H_2), carbon monoxide (CO) or syngas before reaction. The activation process is divided into three parts; the reduction of hematite to metallic iron in hydrogen, followed by the carburization in either syngas or CO and the carburization of hematite with syngas.

2.Experimental

The α-Fe_2O_3 based catalysts were prepared by a combination of precipitation and spray-dried methods [9]. Initially, a corresponding amount of $Fe(NO_3)_3$ solution and NH_4OH solution were added simultaneously to a beaker with pH near 9.0. The temperature was kept at 80 °C during the precipitation process. After repeatedly washed to neutrality, the precipitate was re-slurried and spray-dried. The obtained sample was dried at 120 °C and subsequently calcined at 450 °C for 5 h prior to the experiments.

Environmental transmission electron microscopy (ETEM) experiments were carried out using an aberration corrected and monochromated FEI Titan 80-300 E-cell, operated at 300 kV [37]. Prior to the experiment, the sample was dispersed in ethanol by sonication for 15 min and was drop cast onto a through-hole MEMS heater-chip from DENSsolutions. Iron oxide was reduced *in situ* in hydrogen at elevated temperatures (> 500 °C) at various pressures ~1.3–3.8 mbar. High-pressure studies were carried out using the Climate closed gas-cell holder from DENSsolutions, with a gas flow up to 0.9 NmL/min and a maximum pressure of 1 atm.

In situ X-ray powder diffraction (XRD) patterns were collected on a X'Pert Pro (PANalytical) diffractometer, operating at 45 kV and 40 mA using a Cu(K_α) radiation source (λ = 0.1541 nm). The incident and diffracted beam were filtered through a Ni-foil and a graphite monochromator, respectively Identification of the different iron-containing phases was carried out by a comparison with JCPDF standard spectra software (X'Pert HighScore Plus) or simulated references found in the Inorganic Crystal Structure Database (ICSD) [38]. The reference spectra were simulated in Python, with the packages Pymagten [39] and Xrayutilities [40], where Pymagten is used to create the structures and Xrayutilities is used to simulate the diffraction patterns. A quadrupole mass spectrometer (QMS) mounted on the *in situ* XRD setup was used to follow the change in gas composition, the usage of reactants and the formation of products. The XRD patterns were characterized with Rietveld refinement, which uses a least squares approach by fitting a calculated diffraction pattern to the observed data and was carried out in the software TOPAS (TOtal Pattern Analysis Solution) version 5 from Bruker [41].

X-ray photoelectron spectroscopy (XPS) experiments at the Fe $2p$ edge (709 eV), the O $1s$ edge (530 eV) and the C $1s$ edge (284 eV) with soft X-rays were performed at the ISISS beamline at BESSYII/HZB in Berlin, Germany [42,43]. In this setup, both XPS at near ambient pressure (NAP-XPS) and reflective near edge X-ray absorption fine structure (NEXAFS) spectra in Auger and total electron yield modes are performed simultaneous at elevated pressures (mbar range) with X-ray energies from 80–2000 eV. All measurements were carried out in a stainless-steel NAP-XPS chamber. To reduce charging, the hematite powder sample was pressed into a pellet on an Au-mesh, then mounted on a sapphire sample holder between a stainless-steel backplate and lid with 6 mm hole. The samples were heated from the back using an infrared laser, and the temperature was measured by a type-K thermocouple fastened to the sample surface. The intensity was normalized to the incident photon flux, which was measured using an Au-foil as reference. The binding energies (E_{bin}) were calibrated using the Au $4f_{7/2}$ first order metallic gold peak at 84.0 eV [44]. The accuracy of the E_{bin} calibration was estimated to be around 0.05 eV. All NAP-XPS spectra were analyzed using CasaXPS software from Casa Software Ltd. For metallic iron a Doniach-Sunjic line shape was used whereas for iron oxide's Fe $2p$, O $1s$ and C $1s$ a product of a Gaussian with a Lorentzian line shape was used, all with a Shirley-type background to obtain the best fit.

Both X-ray absorption near-edge spectroscopy (XANES) and extended X-ray absorption fine structure (EXAFS) spectra were measured at the Fe K-edge (7112 eV), in the hard X-rays range. These measurements were carried out at the CAT-ACT beamline at ANKA (the KIT synchrotron) in Karlsruhe, Germany [45]. The hematite sample was diluted with alumina (γ-Al$_2$O$_3$) to achieve the optimal absorption, resulting in an iron content of $\sim$17 wt%. Then, the mixture was pressed into a pellet and sieved to 100–200 μm and loaded into a quartz capillary (1 mm o.d., 0.02 mm wall thickness) reactor with a bed length of 3.5 mm. The experiments are performed with a total flow rate of 29 NmL/min. The raw data were analyzed using the Athena and Artemis extensions of IFEFFIT software [46]. The spectra were merged, energy-calibrated to an Fe-foil and normalized. To evaluate the oxidation state and the chemical nature of Fe species linear combination analysis (LCA) in the range 7100 eV and 7400 eV was performed in Athena [46].

3.Results and discussion

3.1.Reduction of iron oxide

An *in situ* X-ray diffraction experiment was performed in order to determine the temperature range for the different phase transitions taking place during the reduction. In order to mimic ETEM conditions, the H$_2$ flow

controller was set to the minimum of 2 NmL/min and the He was set to the maximum of 140 NmL/min. The exhaust gas was sent to the ambient and thus absolute pressure on the back of the system was 1 atm, corresponding to a H_2 partial pressure of 14 mbar at the sample. The results are shown in Fig. 1.
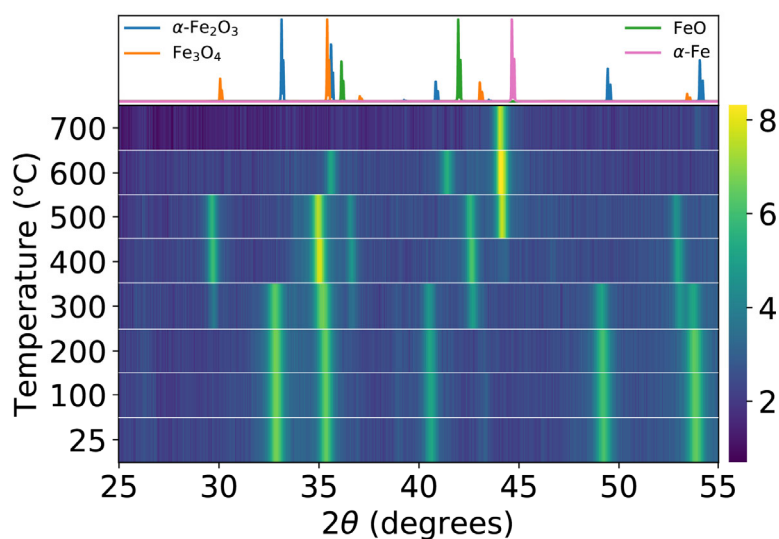

Fig. 1. Intensity plot of XRD patterns from the experiment with partial pressure of 14 mbar (2 NmL/min H_2 in 140 NmL/min He). Each line corresponds to XRD scans taken at different temperatures. The first scan is at 25 °C, the second scan at 100 °C and thereby increasing by 100 °C per scan with a heating rate of 40 °C/min. The top panel is the simulated reference spectra for the bulk compounds.

Four different crystal phases were observed based on a comparison with JCPDF standard spectra software (X'Pert HighScore Plus) and simulated references from the ICSD database. The four phases found during the reduction process are hematite (α-Fe_2O_3) with reflections at 33.2°, 35.5°, 40.8°, 49.5° and 54.2°, magnetite (Fe_3O_4) with reflections at 30.1°, 35.3°, 36.9°, 43.0° and 53.4°, wüstite (FeO) with reflections at 35.8° and 41.7° and lastly metallic iron (α-Fe) with a reflection at 44.8°, occurring over 3 transitions.

$$\alpha\text{-}Fe_2O_3 \rightarrow Fe_3O_4 \rightarrow FeO \rightarrow \alpha\text{-}Fe$$
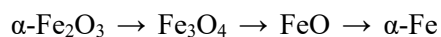
In Fig. S1 in supplementary information, each structure (except wüstite) is singled out at different temperatures from this preliminary experiment, with each structure normalized to the highest peak in the pattern. At room temperature, the sample consists of hematite, at 400 °C the sample is reduced to magnetite, at 600 °C the sample consists of a mixture of wüstite and metallic iron and at 700 °C the sample is completely reduced to metallic iron. The top panel in Fig. 1 is the reference spectra simulated in Python. The reflections in Fig. 1 shift towards lower angles with increasing temperature compared to the simulated reference patterns. This is due to a combination of thermal expansion of the crystal lattice and sample displacement, as the sample shrinks as a result of reduction.

The data from the mass spectrometer of the experiment are shown in Fig. S2 in the supplementary information. The mass spectrometry data show the reduction in accordance with the XRD patterns in Fig. 1. At each temperature increment, both the consumption of hydrogen ($m/q = 2$) as well as the production of water ($m/q = 18$) is observed. The four phases observed during the reduction using *in situ* XRD were further confirmed when reducing hematite in the ETEM. With a pressure of 1.3 mbar H_2 (H_2 flow of 2 NmL/min), hematite was reduced to metallic iron at 500 °C. In order to minimize beam induced effects, the beam was turned off while increasing the temperature between acquiring images and EELS spectra. With limited beam influence, hematite was completely reduced at 500 °C (see Fig. 2). Both images are acquired with a dose rate of 4.6×10^3 e⁻/nm²/s. The crystal structure could not be determined from images at this low magnification. However, at 500°C a reduction in grain size is observed between hematite in Fig. 2(a) and metallic iron in Fig. 2(b). Electron energy-loss spectroscopy (EELS) data support the conclusion that the sample reduces from hematite to metallic iron, see Fig. 3.
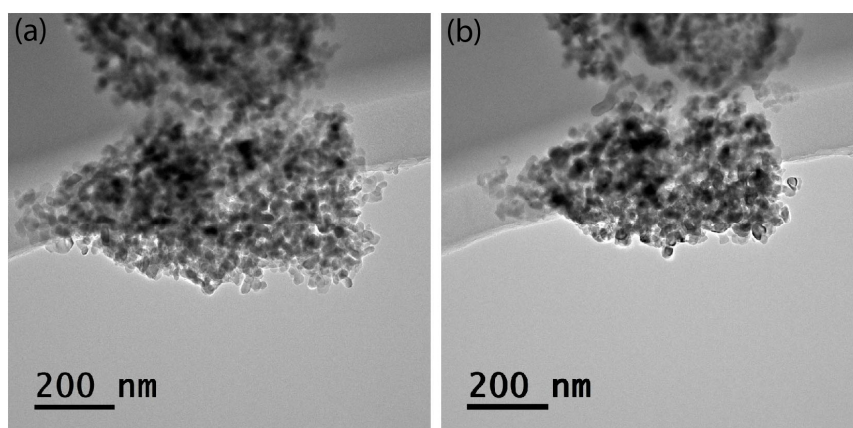

Fig. 2. ETEM images acquired before and after reduction performed at pressure of 1.3 mbar H_2 (H_2 flow of 2 NmL/min), with a dose rate of 4.6×10^3 e⁻/nm²/s, where (a) hematite at 200 °C and (b) metallic iron at 500 °C.
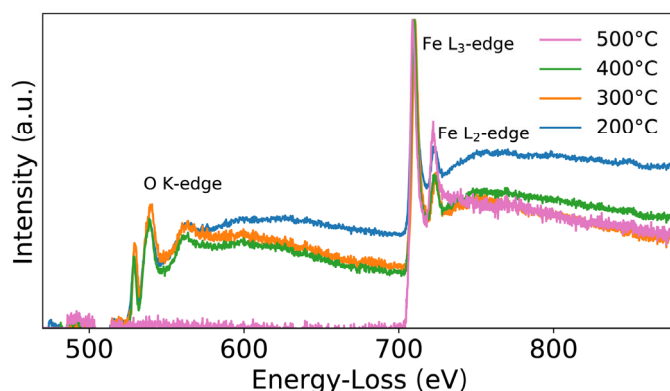
Fig. 3. EELS data from the reduction of hematite at increasing temperatures, showing the oxygen K-edge (~532 eV) and the iron L-edge (~708 eV). The data is normalized at the peak intensity at the Fe L_3-edge.

By following the development of both oxygen K-edges (onset ~532 eV) and iron L-edges (onset ~708 eV), it is possible to determine the oxidation state, see Fig. 3. The raw spectra were deconvoluted using the logarithmic method [47], which assumes that multiple scattering events follow a Poisson distribution. The background was fitted to a power-law and subtracted. The L_3/L_2 intensity ratio was measured as the ratio of the peak areas in the deconvoluted spectra. After background subtraction, a depletion of the oxygen K-edge is observed with increasing temperature in addition to the change in iron L_3/L_2 intensity ratio. The L_3/L_2 intensity ratio goes from 3.6 for hematite [48], 3.4 for magnetite [48] approaching 2 for metallic iron [48]. This indicates that a reduction was taking place, and it was demonstrated that it is possible to reduce hematite in the ETEM at 1.3 mbar H_2.

This was further confirmed in a separate electron diffraction experiment performed at 3.8 mbar H_2 (H_2 flow of 8 NmL/min) (see Fig. 4). The reduction experiment was initiated by raising the temperature to 200 °C and waiting for 15 min., before acquiring a diffraction pattern (Fig. 4a). This process was repeated, while increasing the temperature in steps of 50 °C. At first, no change in the diffraction pattern was observed. Nothing happened until 500 °C, where the first transition to magnetite appeared (Fig. 4b). The next transition to wüstite was observed at 850 °C (Fig. 4c) and the last transition to metallic iron appeared around 1000 °C (Fig. 4d). Even though these transitions took place at significantly higher temperatures than expected from the XRD experiments, which will be commented on later, it was possible to identify each phase by electron diffraction.
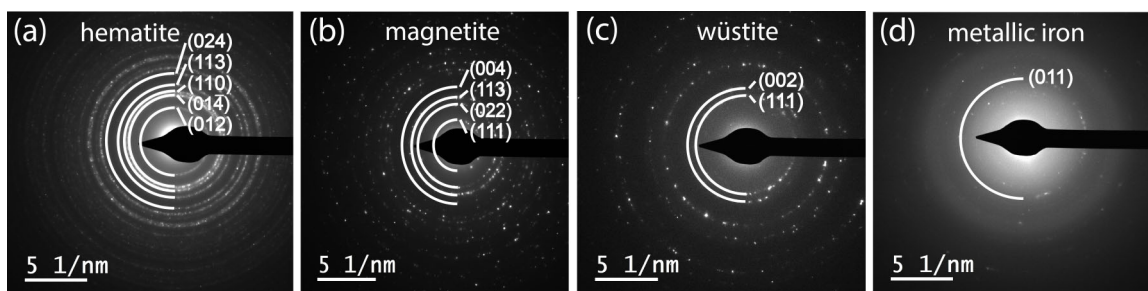
Fig. 4. Electron diffraction patterns of the observed phases during reduction of hematite to metallic iron in 3.8 mbar H₂, where (a) hematite at room temperature, (b) magnetite at 500 °C, (c) wüstite at 850 °C and (d) metallic iron at 1000 °C. The Miller indices indicated in the diffraction patterns refer the identified phases, respectively.

3.2.Temperature dependence

In order to explore the reduction path and rate as a function of temperature, the reduction was performed at varying temperatures under identical conditions by means of *in situ* XRD. The scan time for each scan was decreased to ~15 min by narrowing the range of each scan to 28°–46° (time per step was lowered to 200 ms and the step size was set to 0.026°) The phases of interest all have unique reflections in this range.
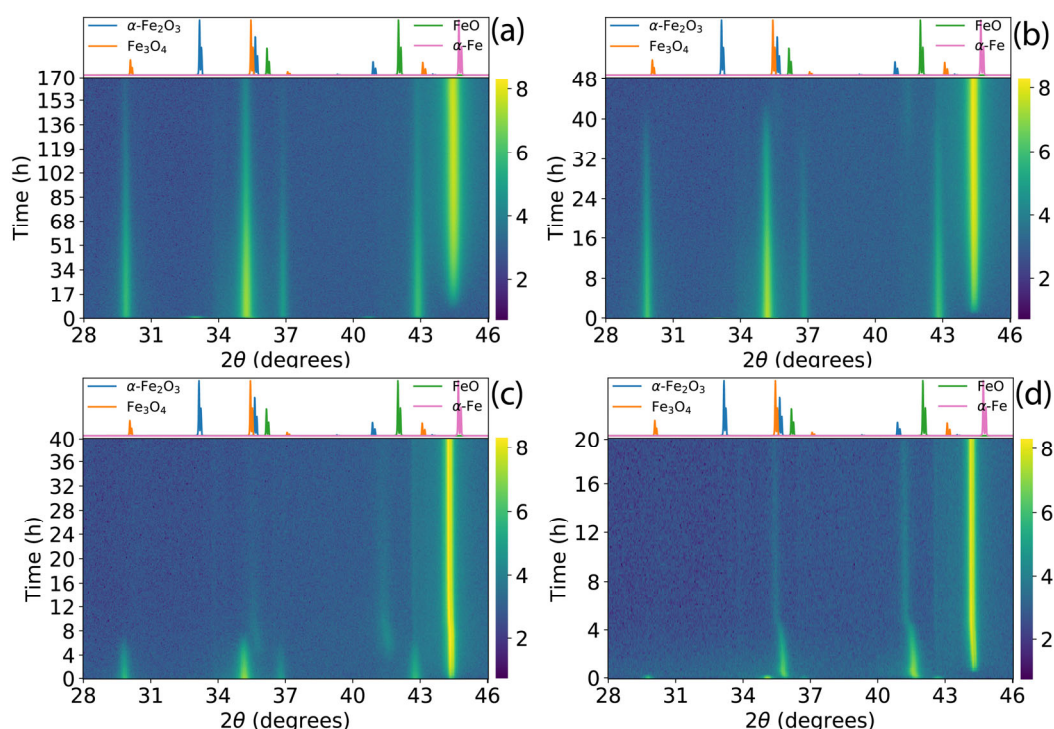

Fig. 5. Intensity plots of the reduction extent over time, taken at different temperatures, where (a) 300 °C, (b) 400 °C, (c) 500 °C and (d) 600 °C. They are all acquired with a partial H₂ pressure of 14 mbar in He and absolute pressure of 1000 mbar. The top panels are the simulated reference spectra for the bulk compounds.

Fig. 5(a) shows data from the experiment conducted at 300 °C and even after 170 h full reduction is still not achieved, as the reflections for magnetite at 30.1°, 35.3°, 36.9° and 43.0° remain. Hematite is reduced to magnetite within the first few scans, as the reflections at 33.2° and 40.8° disappear. The data from the experiment conducted at 400 °C is shown in Fig. 5(b). At this temperature, hematite is reduced to magnetite before the first scan, during the temperature ramp. The sample is considered fully reduced around ~44 hours, as only the reflection for metallic iron is present. Fig. 5(c) shows data from the experiment conducted at 500°C. At this temperature there is no sign of hematite. Magnetite is fully converted to a mixture of wüstite and metallic

iron within 8 hours. However, full conversion of wüstite seems to be a long process and even after 40 h, a trace still remains. Lastly, Fig. 5(d) shows data from the experiment conducted at 600 °C. There is a small trace of magnetite, which is quickly reduced to a mixture of wüstite and metallic iron within the first hour. Like at 500 °C a trace of wüstite remains. The reduction of hematite in H_2 is an exothermic reaction, where the reaction accelerates with increasing temperature. Due to the kinetic limitations, a certain temperature is required to achieve full reduction. This is supported by Niu et al. [8] who shows the H_2-TPR profile of the reduction of hematite in hydrogen, where the reduction takes place in two overall steps: at lower temperature (hematite → magnetite) or higher temperature (magnetite → metallic iron).

Even though it is possible to observe the transition qualitatively, the unequal intensities of the reflections in the different phases make it impossible to obtain any quantitative information. In order to get quantitative phase amounts, a Rietveld refinement was made using TOPAS (see Fig. 6).
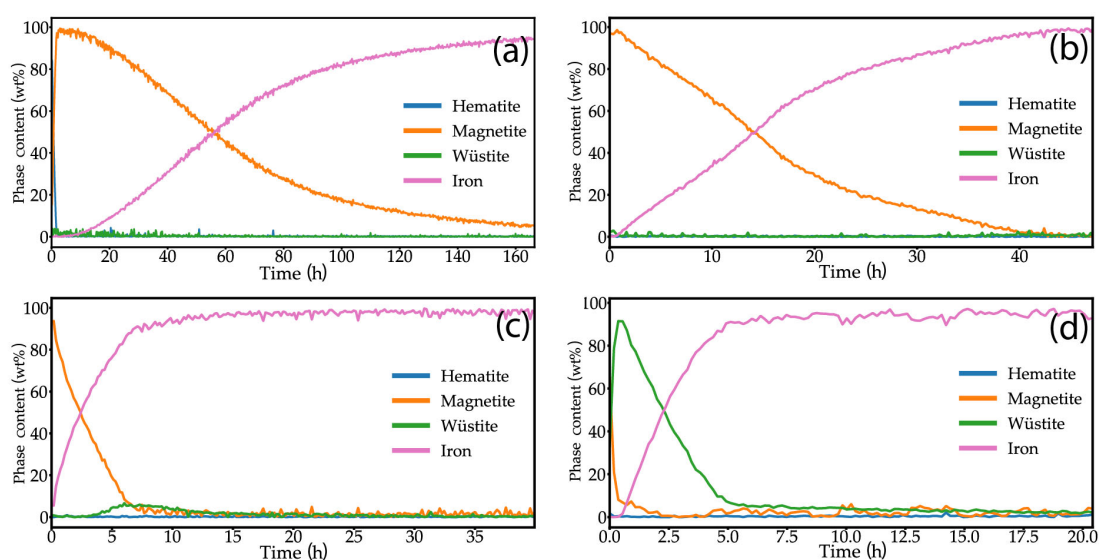

Fig. 6 Rietveld refinements of the reduction extent at different temperatures, where (a) 300 °C, (b) 400 °C, (c) 500 °C and (d) 600 °C.

The Rietveld refinements confirm the observations from above. Fig. 6(a) shows the Rietveld refinement for the experiment conducted at 300 °C, where only a small trace of hematite is present. However, the experiment was terminated before complete reduction was achieved. Fig. 6(b) is the Rietveld refinement for the experiment conducted at 400 °C, where no trace of hematite is observed, and the reduction proceeds from magnetite to metallic iron. Unlike in the intensity plots, the wüstite phase is not visible. Fig. 6(c) is the Rietveld refinement for the experiment conducted at 500 °C, where wüstite can be seen in the beginning. Fig. 6(d) is the Rietveld refinement for the experiment conducted at 600 °C, where a significantly larger contribution of wüstite is observed.

The experiments all show the same trend: the reaction rate increases with increasing temperature, just as the amount of wüstite increases with increasing temperature.
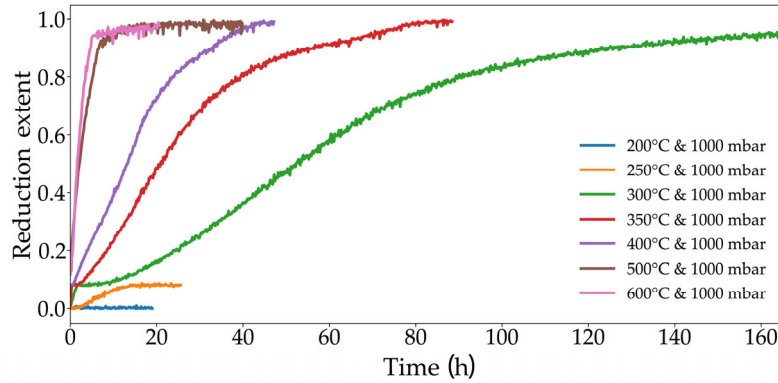

Fig. 7. Temperature dependence of the reduction extent for all experiments.

Fig. 7 shows the reduction extent (χ) based on the Rietveld refinements. χ is a measure of how much of the sample is reduced and is calculated from the amount of oxygen present in the sample from the sample weight (W) and weight of the completely reduced (W_{red}) and oxidized (W_{ox}) sample [49]. The reduction extent is approximated and expressed in terms of weight-% O, with the oxygen content in hematite being 30 wt%.

$$\chi = \frac{W_{ox} - W}{W_{ox} - W_{red}} \approx 1 - \frac{O \text{ wt\%}}{30 \text{ wt\%}}$$

All experiments were conducted at 1000 mbar with varying temperature from 200–600 °C. No reduction takes place at 200 °C. At 250 °C the reduction to magnetite is very clear, but does not proceed from magnetite. Both experiments were stopped after >20 h, since the sample did not reduce any further. At 300 °C and 350 °C the hematite phase is barely visible, but from 400 °C the reduction happens so fast that the hematite phase is impossible to observe. The experiments at 500–600 °C start out as magnetite, as the first transition takes place during temperature ramping.

3.3. Partial pressure dependence

In order to determine the effect of the partial pressure of H_2, a separate set of experiments were performed. As the initial experiment indicated no reduction at temperatures below 200 °C this temperature was chosen as the starting point. The temperature was increased to 700 °C in 10 °C steps, acquiring XRD patterns at every step. The initial experiment is repeated with the above modifications, with as low partial pressure of H_2 as possible

to mimic ETEM conditions. The lowest H_2 flow possible is 2 NmL/min in 140 NmL/min He, resulting in a partial pressure of 14 mbar H_2 and absolute pressure of 1 bar in the system.

Fig. 8(a) shows the XRD patterns from the low H_2 partial pressure of 14 mbar in He, obtained under similar conditions as the experiment in Fig. 1, the only difference is the temperature ramp. The transition between hematite and magnetite occurs at around 300 °C. Further reduction begins around 400 °C, where a reflection around 44° appears, indicating a transition to metallic iron. The reflections from magnetite disappear completely around 550 °C, where small reflections around 36° and 42° emerge, corresponding to wüstite. The reduction is complete at 600 °C, with only one reflection from metallic iron.
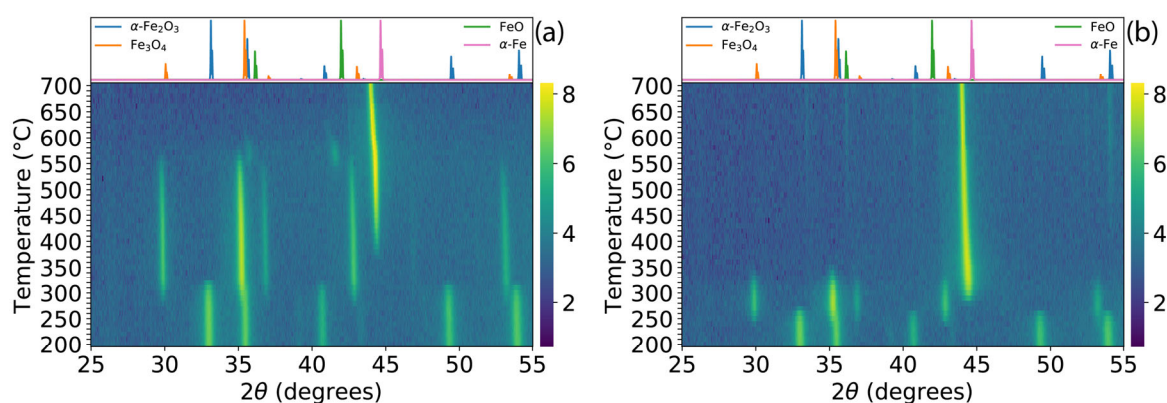

Fig. 8. Intensity plots for different partial pressure, where (a) low partial H_2 pressure of 14 mbar in He and (b) high partial H_2 pressure of 980 mbar in He. The top panels are the simulated reference spectra for the bulk compounds.

Fig. 8(b) shows the XRD patterns from the high H_2 partial pressure of 980 mbar in He. Around 250 °C the first transition from hematite to magnetite takes place. The following transition happens directly from magnetite to metallic iron, without appearance of wüstite. This was expected, as the intermediate wüstite phase only forms at temperatures above 570 °C [23], and since the full reduction has already occurred at 330 °C. The reduction at high H_2 partial pressure is much faster than the reduction at low partial pressure. The sharp peaks at higher temperature in Fig. 8(b) correspond to copper peaks coming from the sample holder, as the amount of sample diminishes at higher temperature, a larger contribution from sample holder arises.

The mass spectrometry data in the supplementary information support what is observed in the XRD patterns. Fig. S3 shows the MS data from low H_2 partial pressure, similar to Fig. S2. The transition from hematite to magnetite occurs around 300 °C, indicated by the consumption of H_2 and the release of water (mass 18). The water signal slowly increases towards a peak and decreases after 12 h, confirming the slower transition to metallic iron observed in the XRD data. The overall water production is much higher at the second step corresponding to higher hydrogen consumption.

The data from the mass spectrometer from the high H_2 partial pressure experiment is seen in Fig. S4. The consumption of H_2 is almost non-visible, whereas the production of water is considerably higher, supporting the fast reduction to metallic iron observed in the XRD patterns.

3.4. Absolute pressure dependence

A series of experiments was performed with reduced absolute pressure at different temperatures in an attempt to better mimic the conditions in the ETEM. Fig. 9 shows the reduction extent during these experiments.
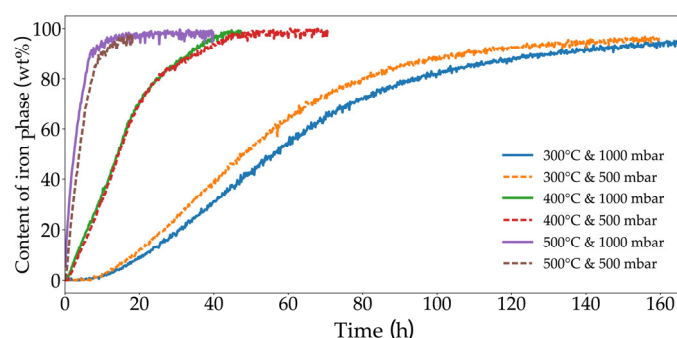

Fig. 9. The content of the iron phase during the reduction performed at both 500 mbar and 1000 mbar, low- and high-absolute pressure, at varying temperature at 300 °C, 400 °C and 500 °C.

Reducing the absolute pressure also reduces the partial pressures, as the 2 NmL/min H_2 in 140 NmL/min He flow is unchanged. Therefore, the reduction process is expected to be slower, since the reduction rate depends on the partial pressure of hydrogen shown above.

Experiments with an absolute pressure of 500 mbar were performed at 300 °C, 400 °C and 500 °C respectively. As expected, the reduction rate is increased when increasing the temperature. However, only a small variation is observed when varying the pressure. At 500 °C, the reaction rate for the experiment at 500 mbar was slightly slower than the experiment at 1000 mbar. At 400 °C, almost no difference is observed and at 300°C a more pronounced increase in reaction rate is observed for the experiment performed at 500 mbar. This could be an effect caused by the water produced during the reaction.

3.5. Grain size dependence

In order to investigate, if the difference in reaction rates at low absolute pressure can be explained by faster removal of water, a series of experiments was made using only half the amount of sample. This is achieved by using a spacer ring to raise the sieve in the Anton Paar cell and loading only half the amount of sample.
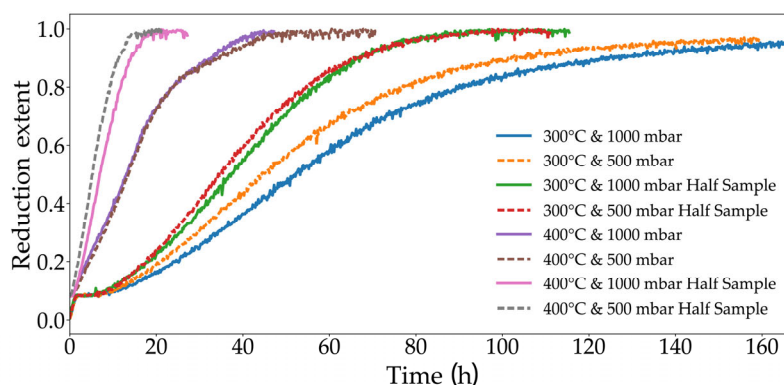
Fig. 10. Reduction extent showing the grain size dependency, of samples at both 300 °C and 400 °C at different absolute pressures at 1000 mbar and 500 mbar repeated with half the amount a sample.

In Fig. 10, the reduction at both 300 °C and 400 °C at different absolute pressures of 1000 mbar and 500 mbar are repeated with half the amount of sample. For experiments performed with half the amount of sample, a significant increase in reaction rate is observed. However, the effect of lowering the absolute pressure seems to have a higher effect at higher temperature. Whereas for lower temperature, the biggest increase in reaction rate when using half a sample is for the highest absolute pressure.
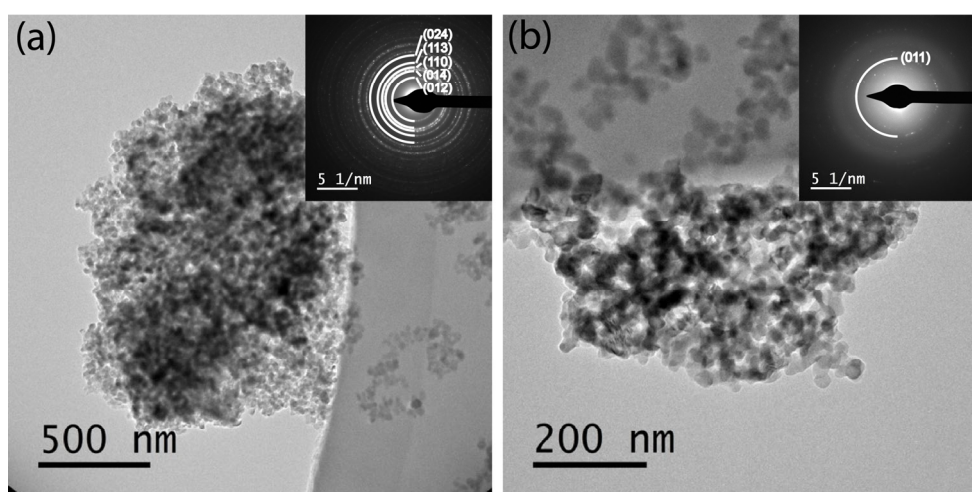

Fig. 11. Two grains of different sizes with corresponding electron diffraction pattern acquired at 450 °C, showing both (a) hematite (hcp) and (b) metallic iron (bcc) present in the sample at the same time.

The increase in the reaction rate is more pronounced for the reaction at 400 °C, which could be explained by a higher water content. As water is produced faster, the partial pressure of water must also be higher and the reduction of the sample should therefore be affected more at higher reduction rates. Thus, the effect of removing half the sample is more pronounced at 400 °C indicating a grain size dependence. An ETEM experiment indicates a similar size dependence. The experiment was started at 200 °C and after 15 min an image and a diffraction pattern were acquired. Then the temperature was increased in steps of 50 °C, and repeated after

14

acquisition. Like earlier, no changes in the diffraction pattern were observed. However, after reaching 450 °C a significant change in the sample had taken place while the electron diffraction pattern remained the same. A small grain was found, and the electron diffraction pattern showed that hematite was completely reduced. In Fig. 11, two grains of different sizes along with corresponding electron diffraction patterns acquired from the entire grain are presented (both acquired at 450 °C). The larger grain in Fig. 11(a) shows hematite and the smaller grain in Fig. 11(b) shows metallic iron. This indicates a grain size dependence, where reduction takes place at higher temperatures for larger grains.

The TEM images show that iron particles are present in grains with varying sizes. The formation of grains of iron particles means that the active site (surface ratio) distribution is inhomogeneous in the iron catalyst, which severely affect the activity and selectivity of the Fischer-Tropsch synthesis. The difference in catalyst performance can be explained by the difference of iron phases formed during the activation process, which can be attributed to the difference in mass-transfer limitations resulting from the difference in grain size. Different grain sizes result in different diffusion length influencing the H_2 or CO profiles during reaction. Thus, the iron phases present are different for the various grain sizes. Furthermore, mass-transfer limitation within a grain can lead to high local conversion where inhibition by water can be magnified by an intraparticle concentration gradient.

3.6. Surface analysis

XPS measurements of Fe 2p, O 1s and C 1s of hematite were carried out. The full experiment can be seen in Fig. S5 in the supplementary information. The XPS peaks of Fe 2$p_{3/2}$ and Fe 2$p_{1/2}$ are shown in Fig. 12(a) where the binding energies of Fe 2$p_{3/2}$ and Fe 2$p_{1/2}$ obtained before reduction at UHV at room temperature is 710.7 eV and 723.8 eV, respectively, corresponding to hematite with a multiplet splitting due to the high spin nature of the Fe^{3+} compounds. The Fe 2p region has a significant spin-orbit splitting of 13.1 eV also visible in the two satellite peaks obtained at 718.6 eV and 731.7 eV, respectively [50,51]. The XPS peaks of O 1s are shown in Fig. 12(b) which can be deconvoluted into two peaks. Herein, the main peak located at about 529.6 eV corresponds to lattice oxygen whereas the minor peak around 531.1 eV corresponds to adsorbed -OH. However, the O 1s peaks cannot be used to determine the oxidation state, as they are very similar for all the relevant Fe-oxides [50]. The XPS peaks of C 1s are shown in Fig. 12(c) with a slight potassium contamination at higher binding energy. Carbon is ubiquitous and is present on all surfaces for XPS analysis.

After the heat treatment in 0.3 mbar H_2 at 700 °C, the reduction of Fe 2p to metallic iron is prominent as the Fe $2p_{3/2}$ and Fe $2p_{1/2}$ peaks shift to 706.4 eV and 719.5 eV, respectively, and the total depletion of O 1s is observed. Furthermore, the C 1s peaks decrease due to contamination burn-off. The Y-axis' for the top and bottom windows (for all spectra) in Fig. 12 is identical for comparison.
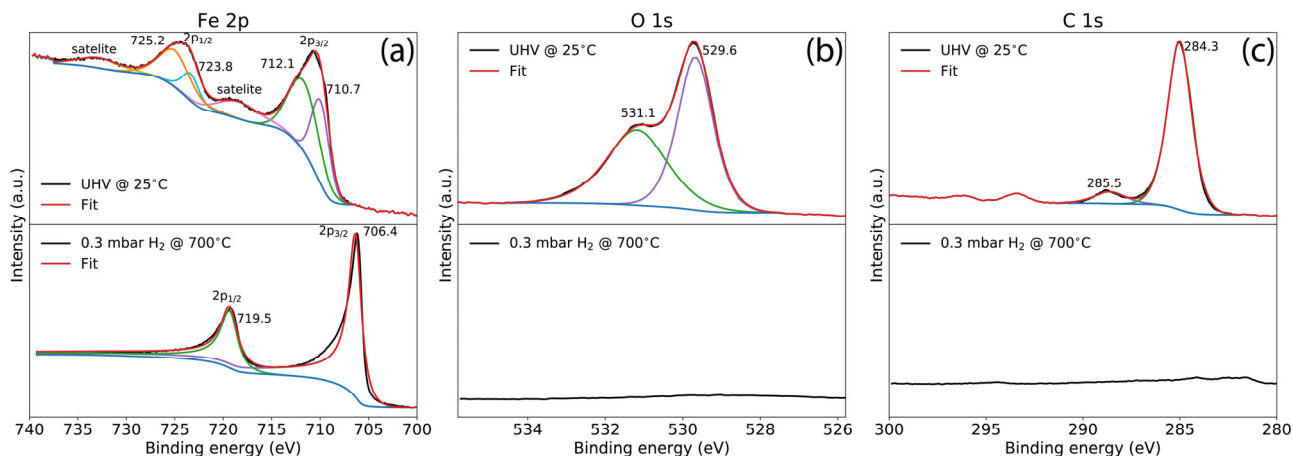

Fig. 12. XPS core-level spectra of the reduction of hematite to metallic iron, where (a) Fe 2p, (b) O 1s and (c) C 1s. The top graph (for all spectra) is taken under UHV at 25 °C and the bottom graph is measured after 2 h reduction in 0.3 mbar H_2 at 700 °C. The Y-axis' are identical for comparison.

In addition to XPS measurements conducted at BESSYII, NEXAFS (Near-Edge X-ray Absorption Fine Structure) measurements in the soft X-ray range were carried out simultaneously. In Fig. 13 spectra of Fe $L_{3,2}$-edges and O K-edges of the iron oxide particles are shown both before reduction at UHV at room temperature and *in situ* in 0.3 mbar H_2 at 700 °C, after assumed reduction taken place. Reference data in Figs. S6 and S7 in supplementary information, for bulk materials, were used to identify specific phases. Prior to the reduction, the Fe L-edge in the NEXAFS spectra in Fig. 13(a) (top panel) is dominated by intense white line features due to *d-p* dipole transitions into unoccupied *d* states. This is due to a combination of crystal field splitting, band formation, spin-orbit coupling and final state exchange interaction. The crystal field splitting of the *d* states can be observed as the splitting of the white line feature related to t_{2g} and e_g final states in the octahedral field. The position of the main L_3-edge peak at 710 eV [52,53], confirms that the starting Fe species are present as a pure Fe^{3+} hematite phase.

The O K-edge in Fig. 13(b) (top panel) shows a double peak in the pre-edge region at 530.1 eV [54], corresponding to the low energy transition from the O *1s* state to the hybridized O *2p*-Fe *3d* state. The second feature just above 540 eV corresponds to O *2p* state hybridized with Fe *4s4p* states.

Increasing the temperature to 700 °C for 2 h resulted in complete reduction to metallic iron, as indicated by the high contribution of the spectral feature at 708.1 eV in addition to the complete depletion of the O K-edge. The Y-axis for the top and bottom windows (for both edges) in Fig. 13 is identical for comparison.
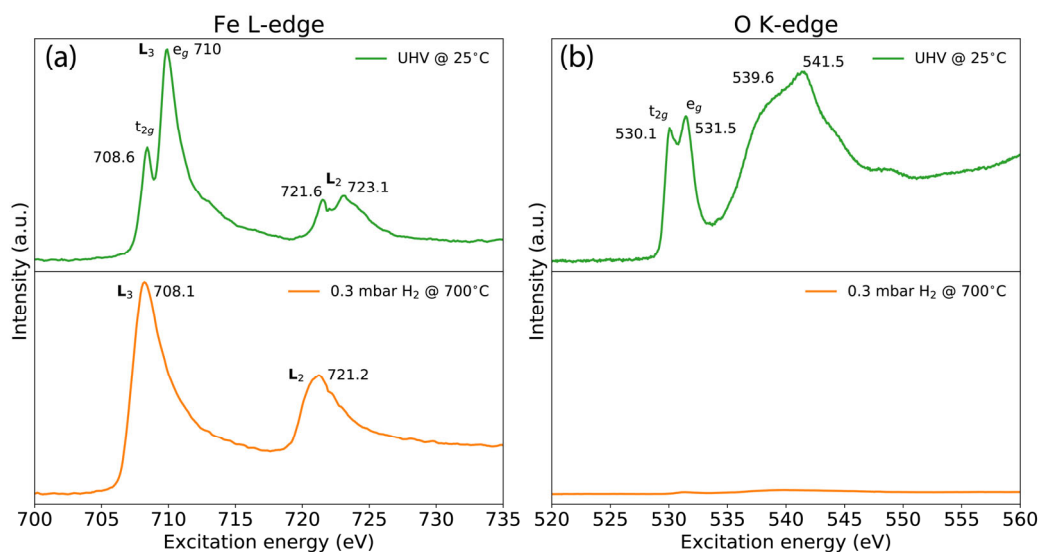

Fig. 13. NEXAFS spectra of the reduction of hematite to metallic iron, for (a) Fe L-edges and (b) O K-edges. The top graphs (for both edges) is taken under UHV conditions at 25 °C and the bottom graph is measured after 2 h reduction in 0.3 mbar H_2 at 700 °C. The Y-axis' are identical for comparison.

Fig. 14(a) shows XANES spectra of the Fe K-edge acquired during the reduction of hematite in 1000 mbar 5% H_2 in He while heating to 630 °C at a ramp of 20 °C/min. The full reduction can be seen in Fig. S8 in the supplementary information. Reference data in Fig. S9 in supplementary information, for bulk materials, were used to identify the specific phases in the experimental data in Fig. 14(b) by comparison. The spectrum measured at room temperature corresponds to hematite, with a pre-edge at 7112.4 eV corresponding to the $1s \rightarrow 3d$ electronic transition, and the main edge ($1s \rightarrow 4p$) transition at 7131.1 eV, both characteristic for hematite [55]. Upon exposure to H_2 and heating, the Fe^{3+} species in the catalyst are reduced to metallic iron, as indicated by the edge position gradually shifting from 7131.1 eV towards 7128.2 eV in addition to the increasing intensity of the pre-edge feature at 7112.4 eV. Even though the catalyst is completely reduced to metallic iron during the temperature ramp, an additional 30 min dwell time at 600 °C is added, to make sure the reaction is complete.
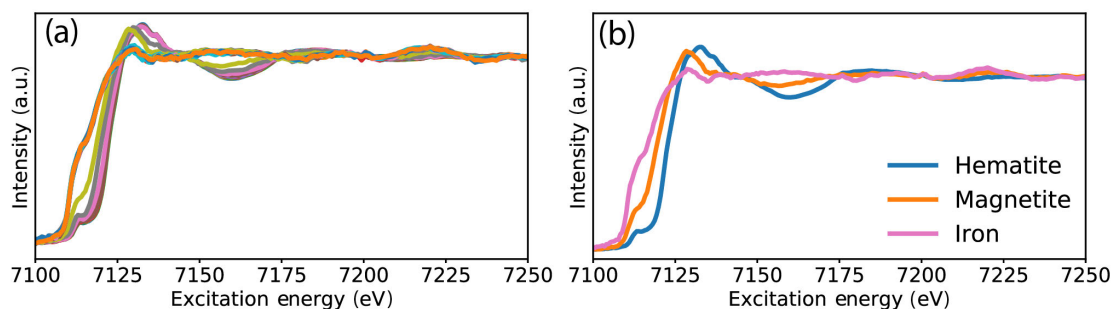
Fig. 14. XANES spectra of the Fe K-edge where (a) is the obtained spectra during the reduction of hematite in 1000 mbar 5% H_2 in He while heating to 630 °C and maintaining for 20 min and (b) is the identified phases: hematite, magnetite and metallic iron.

After identifying the different phases present, least squares linear combination fitting of the XANES spectra was carried out to estimate the phase composition of the sample during the reduction, see Fig. 15. It was possible to identify hematite, magnetite and metallic iron.
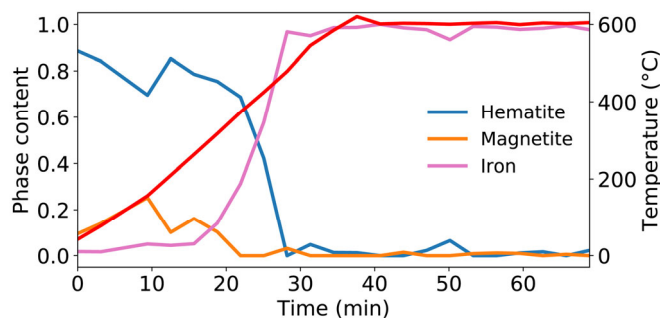

Fig. 15. Linear combination fitting of the *in* situ XANES data to identify the phase composition of hematite (blue), magnetite (orange) and metallic iron (pink) during reduction. The reduction temperature (red) is given on the right axis.

3.7. Carbide formation

3.7.1. Reduction followed by carburization

The carburization process is assumed to occur faster for metallic iron compared to hematite. Therefore, the XRD experiments were separated into the reduction of hematite (in 2 NmL/min H_2 in 140 NmL/min He) followed by the carbide formation at varying H_2/CO ratios. Fig. 16 shows *in situ* XRD data during the H_2/CO treatment after reduction in pure H_2.

In Fig. 16, metallic iron is the starting phase, due to the previous reduction. As iron is carburized, it turns into a mixture of cementite (θ-Fe_3C) and Hägg carbide (χ-Fe_5C_2), which is clear from the Rietveld refinement in Fig. 17. The carburization process seems to be completed during the first few hours, with the disappearance

of the metallic iron phase and the increase in both cementite and Hägg carbide, with Hägg carbide as the dominating carbide at 280 °C. Even after more than 18 hours no further reactions took place. Thus, it is assumed, that no other carbide phases will form. This, combined with the complete depletion of metallic iron phase, indicates that carbide formation takes place in bulk.
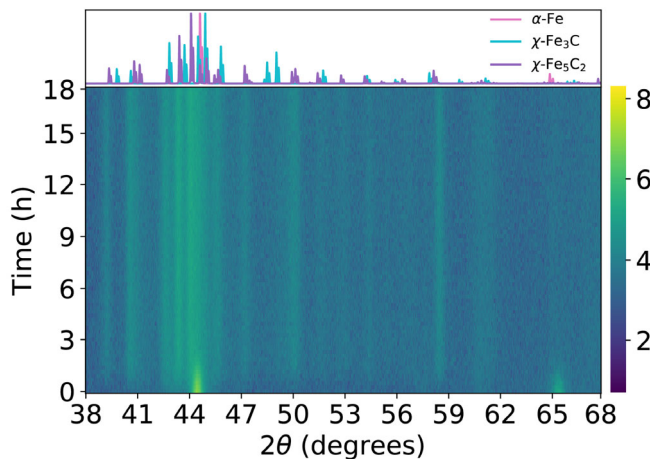

Fig. 16. Intensity plot of the carburization process in a 1/1 H_2/CO ratio (20 mbar H_2/20 mbar CO) in He carried out with an absolute pressure of 1000 mbar at 280 °C. The sample is initially reduced in 14 mbar H_2 (2 NmL/min H_2 in 140 NmL/min He). The top panel is the simulated reference spectra for the bulk compounds.
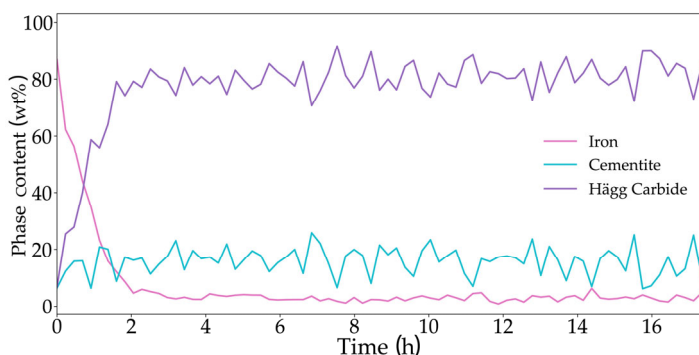

Fig. 17. Rietveld refinement of the carburization process of metallic iron in a 1/1 H_2/CO ratio (20 mbar H_2/20 mbar CO) in He carried out with an absolute pressure of 1000 mbar at 280 °C.

Further experiments were carried out, where the total flow was kept constant, while varying the H_2/CO ratio from 4/1 (80 mbar H_2/20 mbar CO) to 2/1 (40 mbar H_2/20 mbar CO) and 1/1 (20 mbar H_2/20 mbar CO). The reaction rate of carbide formation was observed to increase with increasing H_2/CO ratio and under all conditions, a mixture of cementite and Hägg carbide was formed.

The carburization in NAP-XPS is shown in Fig. 18. The Y-axis are identical to the XPS spectra of the reduction in Fig. 12 (The full experiment can be seen in Fig. S5 in the supplementary information). After the H_2 pre-treatment at 0.3 mbar and 700 °C for 2 h, a H_2/CO ratio was set to 2/1 at 280 °C while acquiring XPS

data, waiting 2 h to make sure no further carburization took place. After no further changes where observed, the temperature was further increased to 310 °C and XPS acquisition was repeated. After carburization for 2 h, the Fe $2p$ peaks in Fig. 18(a) (top panel) shifts towards higher binding energies, and two Fe $2p_{3/2}$ peaks at 709.6 and 711.3 eV and two $2p_{1/2}$ peaks at 722.7 eV and 724.4 eV are observed, with satellite peaks around 715.8 eV and 728.9 eV, respectively. This could indicate the formation of iron carbides [56]. However, this looks similar to wüstite and it is speculated whether a re-oxidation is taking place instead of a carburization, due to the lower pressure the experiments are performed at compared with previously mentioned experiments in the XRD. It further complicates the analysis that O $1s$ peaks in Fig. 18(b) reappears at 530 eV during carburization. When looking at the C $1s$ peaks in Fig. 18(c) small carbon peaks are observed at 285.5 eV and 284.3 eV, respectively [57]. This could further indicate that carbide is being formed. However, it doesn't seem like bulk carbide is formed like it was observed during XRD experiments. This suggests that the formed carbonaceous species, if any, are in the form of a thin surface layer.
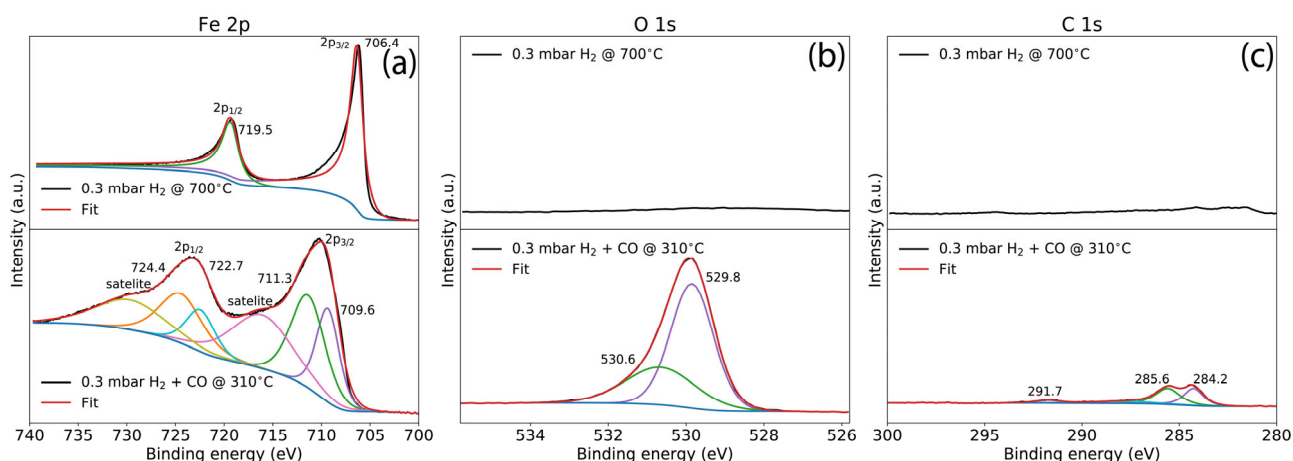

Fig. 18. XPS core-level spectra of the carburization of metallic iron for (a) Fe $2p$, (b) O $1s$ and (c) C $1s$. The top graph (for all spectra) is taken in 0.3 mbar H_2 at 700 °C and the bottom graph is measured in 0.3 mbar of H_2/CO ratio of 2/1 at 310 °C. The Y-axis' are identical for comparison.
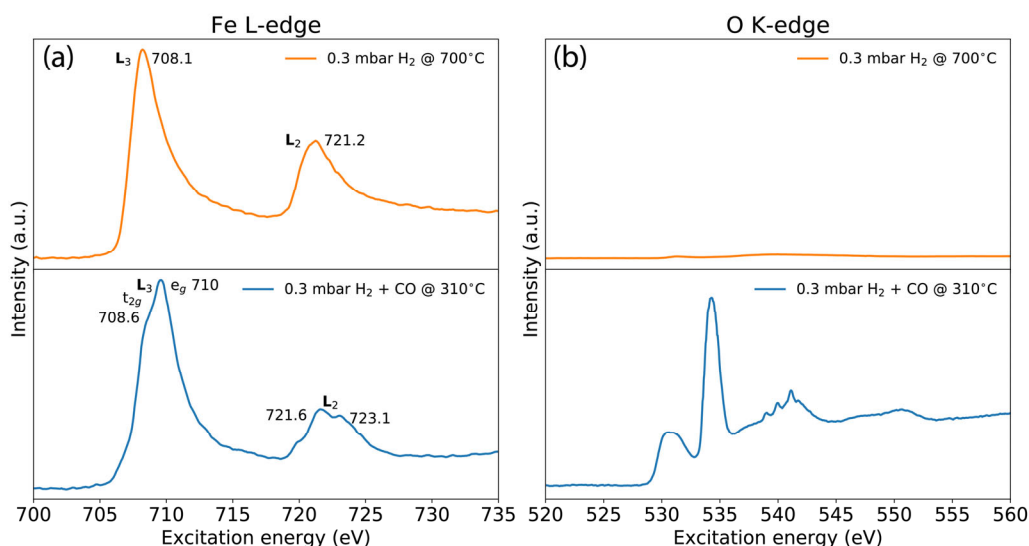
Fig. 19. NEXAFS spectra of the carburization of metallic iron for (a) Fe L-edges and (b) O K-edges. The top graph (for all edges) is taken at 0.3 mbar H_2 at 700 °C and the bottom graph is measured in 0.3 mbar of H_2/CO ratio of 2/1 at 310 °C. The Y-axis' are identical for comparison.

The carburization monitored by NEXAFS is shown in Fig. 19. The Y-axis' are identical to the NEXAFS spectra of the reduction in Fig. 13. The top graph in Fig. 19(a) shows the Fe L-edges for metallic iron at 0.3 mbar H_2 at 700 °C. The bottom spectrum of Fe $2p$ shows a shift to higher excitation energy after carburization at 0.3 mbar H_2/CO ratio of 2/1 at 310 °C. The presence of two almost equivalent components may suggest a mixture of Fe^{2+} and Fe^{3+} [58-60]. A second peak at 708.6 eV is observed, which slowly shifts towards smaller excitation energy. Again, the O K-edge in Fig. 19(b) reappears during carburization. However, just like in the XPS measurement, oxygen is reintroduced into the structure. Combined with the XPS results, which also show a C $1s$ contribution, this could indicate the formation of a very thin layer of carbonaceous species. The large peak at 535 eV is assumed to be the contribution from the gas phase.

3.7.2. Carburization in pure CO

When activating iron oxide in carbon monoxide, see Fig. 20, reduction and carburization take place simultaneously. Fig. 20(a) shows *in situ* XRD data during carburization performed in 14 mbar CO (2 NmL/min CO in 140 NmL/min He) at 400 °C. Fig. 20(b) shows *in situ* XRD data during carburization performed in 20 mbar CO (2 NmL/min CO in 98 NmL/min He) at 280 °C like the previous carburization.
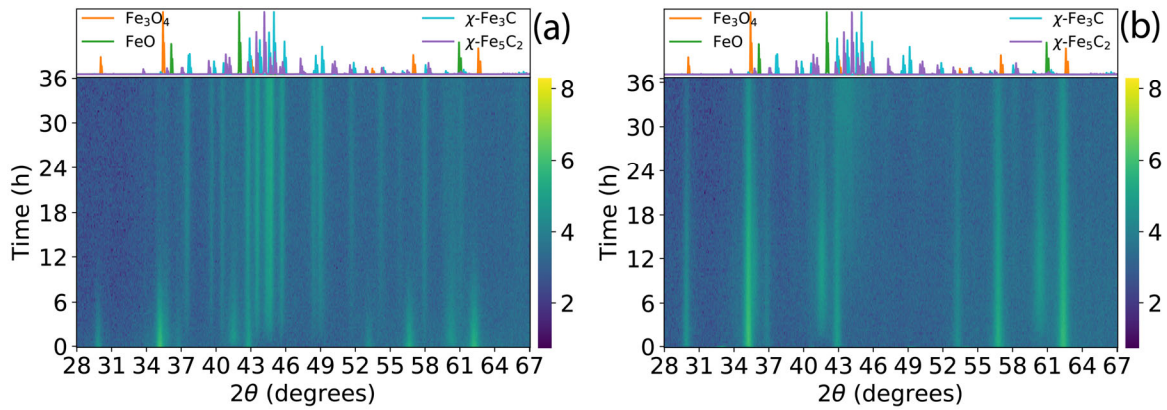
Fig. 20. Intensity plots of the activation of iron oxide in carbon monoxide, where (a) is in 2 NmL/min CO in 140 NmL/min He at 400°C and (b) is in 2 NmL/min CO in 98 NmL/min He at 280 °C. The top panels are the simulated reference spectra for the bulk compounds.

At 14 mbar CO/He at 400 °C, the formation of cementite dominates with an intermediate wüstite phase appearing in the beginning. Iron oxide is completely converted to Hägg carbide within ~15 h, see Fig. 20(a). At 20 mbar CO/He at 280 °C, iron oxide becomes a mixture of magnetite, cementite and Hägg carbide, see Fig. 20(b). Even after 36 h, it doesn't seem like the final carbide phases are reached in the carburization. This is further confirmed by the Rietveld refinement in Fig. 21(a). At 280 °C the reaction rate is much slower and the intermediate wüstite phase is found in higher concentrations. The activation results in a mixture of magnetite and Hägg carbide, with a small amount of cementite, even after 35 h. Whether this is an intermediate towards the other is uncertain. The slope in the Rietveld refinement results, Fig. 21(b), indicates that equilibrium is still not established meaning that the carburization process is still not complete.
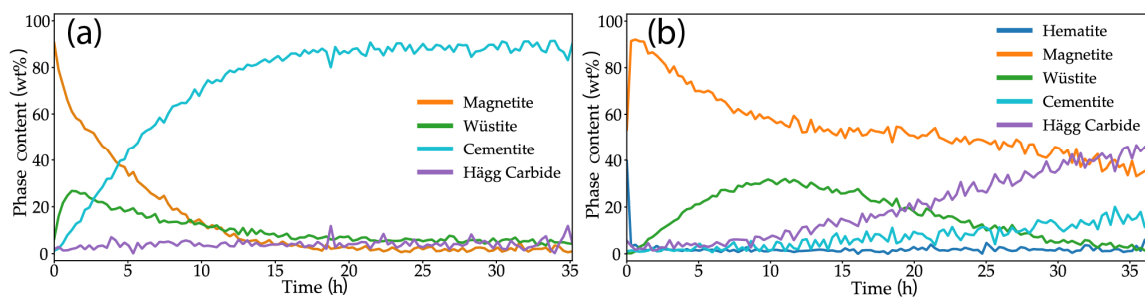

Fig. 21. Rietveld refinement of the activation of iron oxide in carbon monoxide, where (a) is in 2 NmL/min CO in 140 NmL/min He at 400 °C and (b) is in 2 NmL/min CO in 98 NmL/min He at 280 °C.

3.7.3. Carburization in syngas

Carburization of hematite was performed in syngas (4 NmL/min H_2, 2 NmL/min CO in 94 NmL/min He), resulting in a 2/1 H_2/CO ratio at 280 °C (see Fig. 22). From the intensity plot, a slow depletion of magnetite is observed. However, the remaining structures seem undefined or overlapping.
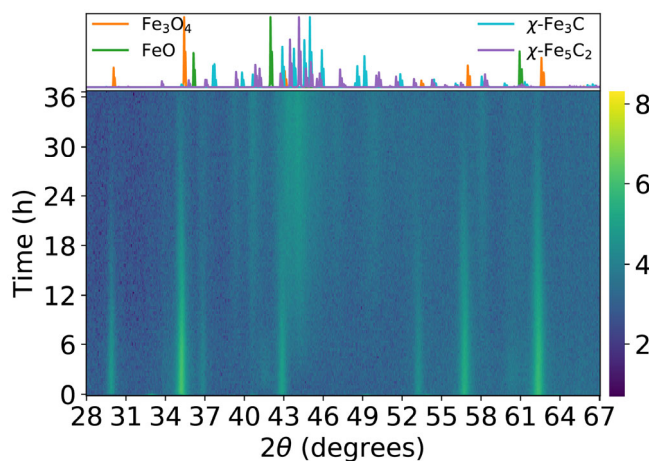

Fig. 22. Intensity plot of the carburization process of hematite in a 2/1 H_2/CO ratio in He carried out at 280 °C with an absolute pressure of 1000 mbar. The top panel is the simulated reference spectra for the bulk compounds.

The Rietveld refinement of the patterns recorded in a syngas-like mixture in Fig. 23 compared with the activation in pure carbon monoxide in Fig. 21 (both conducted at 280 °C), show a difference in the intermediate wüstite phase present during the activation. Furthermore, the activation is assumed complete within ~36 h with the depletion of magnetite, whereas the activating process in pure carbon monoxide in Fig. 21 is still far from reaching the final carbide phase, with a significant amount of magnetite remaining after ~36 h.
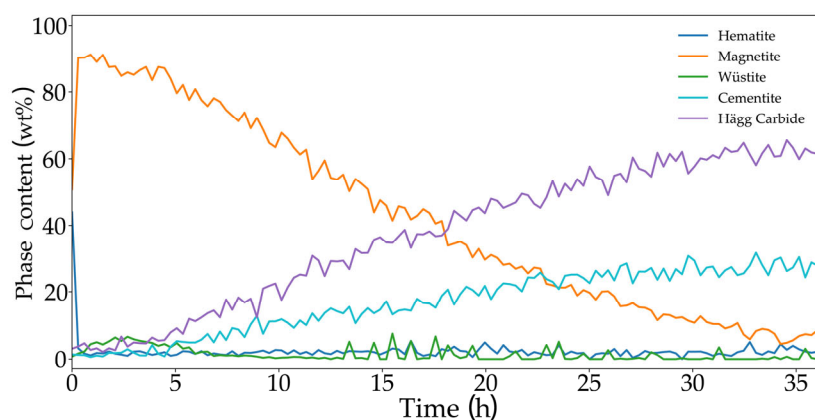

Fig. 23. Rietveld refinement of the carburization process of hematite in a 2/1 H_2/CO ratio in He carried out at 280 °C with an absolute pressure of 1000 mbar.

4.Discussion

Although direct determination of the oxidation state is not possible using XRD, it offers quick identification of the crystalline phases. *In situ* XRD was used to identify the crystallite structures of the four different phases present during activation of hematite. A hexagonal crystal structure corresponding to hematite, a cubic inverse spinel structure assumed to be magnetite, a halite structure corresponding to wüstite and lastly a body-centered cubic structure (bcc) corresponding to metallic iron.

In situ XRD experiments were used to determine at which approximate temperatures transitions take place. Therefore, a steep heating rate was used, where the temperature was increased by steps of 100 °C after each scan of ~60 min, going from 25–700 °C in ~7 h.

A clear difference in the reaction rates between high and low partial H_2 pressure experiments is observed. This is in line with earlier studies, where the hydrogen concentration has been demonstrated to impact the reaction rate [61]. The increased reaction rate of the high partial pressure could be due to the fact, that the reaction is diffusion limited. Comparing the initial experiment with the low partial pressure experiment does, however, not indicate this since both experiments were performed with the same partial pressure, but with different heating rates.

All experiments show a clear increase in reaction rate with increasing temperature. This trend is similar to what has been reported by others [21,22]. However, the reaction rate also depends on the partial pressure of hydrogen and on the water content, which agrees well with previous work [26]. The X_{H2O}/X_{H2} ratio determines whether or not the reduction path occurs in a two step $\alpha\text{-Fe}_2O_3 \rightarrow Fe_3O_4 \rightarrow \alpha\text{-Fe}$ or three step $\alpha\text{-Fe}_2O_3 \rightarrow Fe_3O_4 \rightarrow FeO \rightarrow \alpha\text{-Fe}$ process, if the X_{H2O}/X_{H2} ratio is higher than 0.35, according to Zieliński et al. [23].

Experiments with half the amount of a sample result in to a significant increase in reaction rate. This tendency was observed for experiments both at 300 °C and 400 °C and for experiments performed at different absolute pressures of 500 mbar and 1000 mbar. All showing a clear grain size dependence. It is generally accepted that size and shape influence the reduction kinetics [22]. When the reduction occurs in the gas-solid phase on the surface on the particles, it is previously stated that oxygen diffusion and electron transport inside the particle could be the rate limiting step depending on the morphology. Whereas, for particles in the μm range or larger, the rate limiting step is often due to diffusion [22].

Since XRD does not have the spatial resolution to provide information on the catalyst nanostructure, an environmental TEM was used. Here it was possible to reduce hematite to metallic iron in 1.3 mbar H_2, which was confirmed by EELS with the depletion of the oxygen K-edge and change in the iron L_3/L_2 intensity ratio.

This is similar to earlier studies, where the evolution of iron oxide was visualized during reaction in an ETEM [62]. Furthermore, the individual phases were determined with electron diffraction, which supports the grain size dependence mentioned above as differently sized grains showed different stages of the reduction. This could be explained by a heat transfer problem between the MEMS chip and grain, preventing larger grains from reaching the temperature needed for the reduction to take place. Other possible explanations could be an effect caused by the water produced during the reaction bringing the local concentration of water higher damping the reduction or a shortage of reactive gas in the large reaction chamber in the ETEM (~800 cm^3). The latter is, however, very unlikely as the sample/gas ratio is much larger with only a few micrograms of hematite dispersed on a MEMS chip. However, in combination with the XRD finding, it is most likely due to the presence of water created during the reduction blocking access to the reactive sites, decreasing the reaction rate. This is more pronounced in the ETEM data, due to the limited gas flow of 2 NmL/min which may not evacuate the product gas efficiently around the iron oxide particles. This effect of water decreases at high temperature.

As ETEM experiments give a local idea of what is going on and XRD and hard X-ray XAS provide bulk information, but little information about the chemical nature of the iron surfaces (or formed surfaces) during activation, therefore surface-sensitive techniques such as XPS and soft X-ray XAS were used. With XPS, it was possible to confirm both metallic iron and iron oxide species, with peak positions corresponding to hematite being the starting point, with the addition of carbon contamination. After reduction, metallic iron is confirmed with the depletion of the oxygen peak. This was further confirmed by XAS.

Common to all XRD carburization experiments, regardless of the iron starting phase and carburization conditions, are the complete conversion into bulk iron carbide. The final iron carbide products vary, nevertheless, the iron oxide or metallic iron is completely converted into bulk iron carbide, with the exception of the carburization experiment in pure CO at 280 °C, which still contain magnetite. However, the slope in the Rietveld refinement tells us that equilibrium is still not established and the activating process is not complete. It is therefore assumed that with a sufficient time the magnetite phase will completely disappear like in the other carburization experiments.

The carburization process from metallic iron leads to a mixture of Hägg carbide (χ-Fe$_5$C$_2$) and cementite (θ-Fe$_3$C), which agrees well with previous work [7,9]. Regardless of the H$_2$/CO ratio used during the carburization experiment, it leads to a 4/1 Hägg carbide/cementite ratio. The carburization process from hematite is considerably slower, with magnetite being present during most of the reaction. However, this

reaction also results in a combination of Hägg carbide and cementite, with a slightly different ratio closer to 3/1 Hägg carbide/cementite ratio. Activating hematite in pure CO at 280 °C results in a significant amount of the intermediate wüstite phase. This experiment indicates that the wüstite phase is an inhibiting intermediate towards the formation of iron carbide, as the concentration of the carbides does not seem to increase until the concentration of wüstite decreases. This can, however, be due to the influence of water, as it is well known that wüstite is formed when there is a high water content. Activating hematite in pure CO at 400 °C resulted in a smaller amount of wüstite, which is removed much faster during the reaction, resulting in almost pure cementite also indicating that the final iron carbide composition has a temperature dependence. The formation of Hägg carbide is favored for the experiments at 280 °C while cementite is favored at 400 °C.

The nature of the iron catalyst, i.e. whether it is reduced or not, and the carburization conditions play an important role in the process of determining which iron carbide, or combination of iron carbides, is formed at different reaction conditions. Furthermore, it seems that there is a general loss of crystallinity after carburization, which might be explained by the fact that XRD only detects crystalline structures. However, octahedral iron carbides are often either amorphous, which are not visible in the XRD, or contain very small crystal structures that are difficult to detect due to peak broadening.

After carburization for 2 h in 0.3 mbar 2/1 H_2/CO ratio, the Fe $2p_{3/2}$ and $2p_{1/2}$ peaks shift towards higher binding energy, at 709.6 eV and 722.7 eV, respectively. This could correspond to wüstite in addition to the O $1s$ peak at 284.4 eV reappearing. However, since two small carbon peaks appear in the C $1s$ spectrum at 285.5 and 284.4 eV, it could indicate that a small amount of carbonaceous species is formed. In the XRD experiments bulk iron carbide is formed, but in XPS it is more likely that carbonaceous species are formed on the surface. This is similar to what has been reported by others [57]. However, these experiments were performed at different conditions, and are therefore not directly comparable.

5.Conclusions

In situ characterization techniques were used to a gain a better understanding of the various iron species present during the activation phase of an iron-based FTS catalyst.

In situ XRD was used to identify the crystalline phases present during activation of hematite. A clear increase in reaction rate with increasing temperature was established. The hydrogen concentration was demonstrated to impact the reduction rate, by varying both the partial and absolute H_2 pressure. Additionally,

the water content impacts the activation, and the X_{H2O}/X_{H2} ratio determine whether the reduction path occurs in a two or three step process.

In the ETEM, a complete reduction was demonstrated. Furthermore, a dependence on grain size on the reducibility was established, i.e. bigger grains require higher temperature to reduce. It is suggested that the local production of water is the reason, as the water content was demonstrated to have a high effect.

XPS and XAS both indicate that a small amount of carbonaceous species is formed at the surface of the bulk metallic iron. This is in contrast to the XRD experiments that show the formation of bulk iron carbide.

Acknowledgments

References

[1]   H. Schulz, *Appl. Catal. A* 186, (1999) 3-12.
[2]   B. H. Davis, *Catal. Today* 84, (2003) 83-98.
[3]   M. E. Dry, *Journal of Chemical Technology and Biotechnology* 77, (2002) 43-50.
[4]   N. Koizumi, K. Murai, T. Ozaki, M. Yamada, *Catal. Today* 89, (2004) 465-478.
[5]   M. E. Dry, *Catal. Today* 71, (2002) 227-241.
[6]   T. A. Wezendonk, X. Sun, A. I. Dugulan, A. J. F. van Hoof, E. J. M. Hensen, F. Kapteijn, J. Gascon, *J. Catal.* 362, (2018) 106-117.
[7]   E. de Smit, F. Cinquini, A. M. Beale, O. V. Safonova, W. van Beek, P. Sautet, B. M. Weckhuysen, *J. Am. Chem. Soc.* 132, (2010) 14928-14941.
[8]   L. W. Niu, X. W. Liu, X. Liu, Z. G. Lv, C. H. Zhang, X. D. Wen, Y. Yang, Y. W. Li, J. Xu, *ChemCatChem* 9, (2017) 1691-1700.
[9]   L. Niu, X. Liu, J. Liu, X. Liu, X. Wen, Y. Yang, J. Xu, Y. Li, *J. Catal.* 371, (2019) 333-345.
[10]   P. M. Maitlis, V. Zanotti, *Chem Commun (Camb)*, (2009) 1619-1634.
[11]   D. S. Newsome, *Catalysis Reviews* 21, (1980) 275-318.
[12]   H.-b. Zhang, G. L. Schrader, *J. Catal.* 95, (1985) 325-332.

[13]   D. G. Rethwisch, J. A. Dumesic, *J. Catal.* 101, (1986) 35-42.

[14]   E. S. Lox, G. F. Froment, *Ind. Eng. Chem. Res.* 32, (1993) 71-82.

[15]   K. R. P. M. Rao, F. E. Huggins, V. Mahajan, G. P. Huffman, V. U. S. Rao, *Hyperfine Interactions* 93, (1994) 1745-1749.

[16]   K. Rao, F. E. Huggins, V. Mahajan, G. P. Huffman, V. U. S. Rao, B. L. Bhatt, D. B. Bukur, B. H. Davis, R. J. Obrien, *Top. Catal.* 2, (1995) 71-78.

[17]   F. Blanchard, J. P. Reymond, B. Pommier, S. J. Teichner, *Journal of Molecular Catalysis* 17, (1982) 171-181.

[18]   C. S. Kuivila, P. C. Stair, J. B. Butt, *J. Catal.* 118, (1989) 299-311.

[19]   J. P. Reymond, P. Mériaudeau, S. J. Teichner, *J. Catal.* 75, (1982) 39-48.

[20]   E. Lorente, J. Herguido, J. A. Peña, *International Journal of Hydrogen Energy* 36, (2011) 13425-13434.

[21]   A. Pineau, N. Kanari, I. Gaballah, *Thermochim. Acta* 447, (2006) 89-100.

[22]   O. J. Wimmers, P. Arnoldy, J. A. Moulijn, *J. Phys. Chem.* 90, (1986) 1331-1337.

[23]   J. Zieliński, I. Zglinicka, L. Znak, Z. Kaszkur, *Appl. Catal. A-Gen.* 381, (2010) 191-196.

[24]   W. K. Jozwiak, E. Kaczmarek, T. P. Maniecki, W. Ignaczak, W. Maniukiewicz, *Appl. Catal. A-Gen.* 326, (2007) 17-27.

[25]   G.-Y. Lee, J.-l. Song, J.-S. Lee, *Powder Technology* 302, (2016) 215-221.

[26]   P. Thüne, P. Moodley, F. Scheijen, H. Fredriksson, R. Lancee, J. Kropf, J. Miller, J. W. Niemantsverdriet, *The Journal of Physical Chemistry C* 116, (2012) 7367-7373.

[27]   H. Rau, *The Journal of Chemical Thermodynamics* 4, (1972) 57-64.

[28]   I. Barin, O. Knacke, *Thermochemical Properties of Inorganic Substances*.   (Springer, ed. 1, 1973).

[29]   A. Kock, J. W. Geus, *Progress in Surface Science* 20, (1985) 165-272.

[30]   R. B. Levy, M. Boudart, *Science* 181, (1973) 547-549.

[31]   S. T. Oyama, *Catal. Today* 15, (1992) 179-200.

[32]   J. G. Chen, *Chem. Rev.* 96, (1996) 1477-1498.

[33]   J. M. Gracia, F. F. Prinsloo, J. W. Niemantsverdriet, *Catal. Lett.* 133, (2009) 257-261.

[34]   J. W. Niemantsverdriet, A. M. van der Kraan, *J. Catal.* 72, (1981) 385-388.

[35]   E. de Smit, B. M. Weckhuysen, *Chemical Society reviews* 37, (2008) 2758-2781.

[36]   M. D. Shroff, A. K. Datye, *Catal. Lett.* 37, (1996) 101-106.

[37]   T. W. Hansen, J. B. Wagner, R. E. Dunin-Borkowski, *Mater. Sci. Technol.* 26, (2010) 1338-1344.

[38]   http://www.fizkarlsruhe.de/icsd.html.

[39]   S. P. Ong, W. D. Richards, A. Jain, G. Hautier, M. Kocher, S. Cholia, D. Gunter, V. L. Chevrier, K. A. Persson, G. Ceder, *Comp. Mater. Sci* 68, (2013) 314-319.

[40]   D. Kriegner, E. Wintersberger, J. Stangl, *J. Appl. Crystallogr.* 46, (2013) 1162-1170.

[41]   A. A. Coelho, *J. Appl. Crystallogr.* 51, (2018) 210-218.

[42]   A. Knop-Gericke, E. Kleimenov, M. Havecker, R. Blume, D. Teschner, S. Zafeiratos, R. Schlogl, V. I. Bukhtiyarov, V. V. Kaichev, I. P. Prosvirin, A. I. Nizovskii, H. Bluhm, A. Barinov, P. Dudin, M. Kiskinova, in *Advances in Catalysis, Vol 52,* B. C. Gates, H. Knozinger, Eds. (Elsevier Academic Press Inc, San Diego, 2009), vol. 52, pp. 213-272.

[43]   A. Klyushin, R. Arrigo, V. Pfeifer, T. Jones, J. Velasco Vélez, A. Knop-Gericke, in *Encyclopedia of Interfacial Chemistry,* K. Wandelt, Ed. (Elsevier, Amsterdam, 2018), pp. 615-631.

[44]   A. Y. Klyushin, T. C. R. Rocha, M. Havecker, A. Knop-Gericke, R. Schlogl, *Phys. Chem. Chem. Phys.* 16, (2014) 7881-7886.

[45] A. Zimina, K. Dardenne, M. A. Denecke, D. E. Doronkin, E. Huttel, H. Lichtenberg, S. Mangold, T. Pruessmann, J. Rothe, T. Spangenberg, R. Steininger, T. Vitova, H. Geckeis, J. D. Grunwaldt, *Rev. sci. Instrum.* 88, (2017) 16.

[46] B. Ravel, M. Newville, *J. Synchrot. Radiat.* 12, (2005) 537-541.

[47] D. W. Johnson, J. C. H. Spence, *Journal of Physics D-Applied Physics* 7, (1974) 771-780.

[48] T. G. Sparrow, B. G. Williams, C. N. R. Rao, J. M. Thomas, *Chemical Physics Letters* 108, (1984) 547-550.

[49] G. Y. Lee, J. I. Song, J. S. Lee, *Powder Technology* 302, (2016) 215-221.

[50] C. J. Jia, L. D. Sun, F. Luo, X. D. Han, L. J. Heyderman, Z. G. Yan, C. H. Yan, K. Zheng, Z. Zhang, M. Takano, N. Hayashi, M. Eltschka, M. Klaui, U. Rudiger, T. Kasama, L. Cervera-Gontard, R. E. Dunin-Borkowski, G. Tzvetkov, J. Raabe, *J. Am. Chem. Soc.* 130, (2008) 16968-16977.

[51] C. Y. Guo, F. Y. Xia, Z. Wang, L. Zhang, L. Xi, Y. L. Zuo, *Journal of Alloys and Compounds* 631, (2015) 183-191.

[52] F. d. Groot, A. Kotani, *Core Level Spectroscopy of Solids*. (Taylor & Francis, Boca Raton, ed. 1, 2008).

[53] W. M. Heijboer, A. A. Battiston, A. Knop-Gericke, M. Havecker, R. Mayer, H. Bluhm, R. Schlogl, B. M. Weckhuysen, D. C. Koningsberger, F. M. F. de Groot, *J. Phys. Chem. B* 107, (2003) 13069-13075.

[54] F. M. F. de Groot, M. Grioni, J. C. Fuggle, J. Ghijsen, G. A. Sawatzky, H. Petersen, *Phys. Rev. B* 40, (1989) 5715-5723.

[55] M. Wilke, F. o. Farges, P.-E. Petit, G. E. Brown, Jr., F. o. Martin, *American Mineralogist* 86, (2001) 714-730.

[56] A. Furlan, U. Jansson, J. Lu, L. Hultman, M. Magnuson, *J Phys Condens Matter* 27, (2015) 045002.

[57] F. Bonnet, F. Ropital, P. Lecour, D. Espinat, Y. Huiban, L. Gengembre, Y. Berthier, P. Marcus, *Surf. Interface Anal.* 34, (2002) 418-422.

[58] S. L. Yang, D. N. Wang, G. X. Liang, Y. M. Yiu, J. J. Wang, L. J. Liu, X. L. Sun, T. K. Sham, *Energy & Environmental Science* 5, (2012) 7007-7016.

[59] A. Koehl, D. Kajewski, J. Kubacki, C. Lenser, R. Dittmann, P. Meuffels, K. Szot, R. Waser, J. Szade, *Phys. Chem. Chem. Phys.* 15, (2013) 8311-8317.

[60] M. Gimenez-Marques, E. Bellido, T. Berthelot, T. Simon-Yarza, T. Hidalgo, R. Simon-Vazquez, A. Gonzalez-Fernandez, J. Avila, M. C. Asensio, R. Gref, P. Couvreur, C. Serre, P. Horcajada, *Small* 14, (2018) 11.

[61] L. Guo, H. Gao, J. T. Yu, Z. L. Zhang, Z. C. Guo, *Int. J. Miner. Metall. Mater.* 22, (2015) 12-20.

[62] X. Liu, C. H. Zhang, Y. W. Li, J. W. Niemantsverdriet, J. B. Wagner, T. W. Hansen, *ACS Catal.* 7, (2017) 4867-4875.

TOC: Iron oxide is a precursor for iron-based Fischer-Tropsch synthesis catalysts. The reduction and carburization processes can result in a plethora of phases.

Fe L₃-edge

Fe L₂-edge

	500°C
	400°C
	300°C
	200°C

600   700   800
Energy-Loss (eV)